RESEARCH ARTICLE
SPACE PHYSICS: IONOSPHERIC PHYSICS

Earth and Planetary Physics
5: 397–406, 2021
doi: 10.26464/epp2021045

Interaction between Equatorial Plasma Bubbles and a Medium-Scale Traveling Ionospheric Disturbance, observed by OI 630 nm airglow imaging at Bom Jesus de Lapa, Brazil

Cristiano Max Wrasse[1*], Cosme Alexandre Oliveira Barros Figueiredo[1], Diego Barros[1], Hisao Takahashi[1], Alexander José Carrasco[2], Luiz Fillip Rodrigues Vital[1], Láysa Cristina Araujo Resende[1,3], Fábio Egito[4], Geângelo de Matos Rosa[5], and Antonio Hélder Rodrigues Sampaio[5]

[1]Space Weather Division, National Institute for Space Research (INPE), São José dos Campos, Brazil;

[2]University of Los Andes (ULA), Mérida, Venezuela;

[3]State Key Laboratory of Space Weather, Beijing 100190, China;

[4]Federal University of Campina Grande (UFCG), Campina Grande, Brazil;

[5]Federal Institute for Education, Science and Technology Baiano (IF Baiano), Bom Jesus da Lapa, Brazil

Key Points:

- Observational evidence of interaction between Equatorial Plasma Bubble and Medium-Scale Traveling Ionospheric Disturbance (MSTID) at low latitude over Brazilian.
- Electric fields associated with MSTID can intensify the growth of the Equatorial Plasma Bubble.
- Partial inhibition of the Equatorial Plasma Bubble by MSTID occurs after the bubble intensifies and bifurcates.

Citation: Wrasse, C. M., Figueiredo, C. A. O. B., Barros, D., Takahashi, H., Carrasco, A. J., Vital, L. F. R., Rezende, L. C. A., Egito, F., Rosa, G. M., and Sampaio, A. H. R. (2021). Interaction between Equatorial Plasma Bubbles and a Medium-Scale Traveling Ionospheric Disturbance, observed by OI 630 nm airglow imaging at Bom Jesus de Lapa, Brazil. *Earth Planet. Phys.*, *5*(5), 397–406. http://doi.org/10.26464/epp2021045

Abstract: OI 630.0 nm airglow observations, from a new observatory at Bom Jesus de Lapa, were used to study the interaction between EPBs (Equatorial Plasma Bubbles) and the MSTID (Medium- Scale Traveling Ionospheric Disturbance) over the Northeast region in Brazil. On the night of September 16 to 17, 2020, an EPB was observed propagating eastward, in an apparent fossil stage, until it interacted with a dark band electrified MSTID (eMSTID). After the interaction, four EPBs merged, followed by an abrupt southward development and bifurcations. Analysis of the data suggests that an eastward polarization electric field, induced by the dark band eMSTID, forced the EPB into an upward drift, growing latitudinally along the magnetic field lines and then bifurcating.

Keywords: Equatorial Plasma Bubbles; Medium-Scale Traveling Ionospheric Disturbance; ionosphere; thermosphere; EPB and MSTID interaction

1. Introduction

Equatorial plasma depletions related to density irregularities often occur in the nighttime ionosphere at low and mid-latitudes (Katamzi-Joseph et al., 2017). The ionospheric plasma depletions, called Equatorial Plasma Bubbles (EPBs) or spread-F, are initiated by instability in the bottom side F-region of the equatorial ionosphere (Abdu, 2001). The gravitational force and density gradient are antiparallel in the F-region's bottom side, resulting in Rayleigh–Taylor instability (Haerendel, 1973; Kelley, 2009). During the development, EPBs drift eastward with a velocity ranging from ~50 to 200 m/s and rise to altitudes of ~400 to 2000 km over the magnetic equator (Sobral et al., 1981; Pimenta et al., 2003; Barros et al., 2018).

In the context of the Rayleigh–Taylor mechanism, the ionosphere can be described by several thin layers of different densities. Occurrence of a perturbation in the interface between two fluids (a heavy fluid over a light one) can lead to development of instabilities and can generate EPBs. The polarization electric field produced inside an EPB maps simultaneously to both hemispheres, causing an elongation of the EPB along the magnetic field lines (Sobral et al., 2009; Otsuka et al., 2002). The vertical growth of the flux tube-aligned plasma depletions over the equator, with the associated smaller-scale structure, is responsible for the spread F latitudinal extension (the EPB). Its occurrence in a low latitude station can indicate the vertical EPB extension to the equatorial apex height of the field line that maps to the F layer bottom side over these stations (Abdu et al., 1983; 2009). During quiet times, EPBs

Correspondence to: C. M. Wrasse, cristiano.wrasse@inpe.br
Received 13 APR 2021; Accepted 02 AUG 2021.
Accepted article online 19 AUG 2021.

can reach the geographic latitude of ±35°, depending on their Apex height (Pimenta et al., 2003; Barros et al., 2018; Carrasco et al., 2017). On the other hand, under some extreme cases during geomagnetically storm conditions, EPBs can extend to latitudes greater than 40° (e.g., Huang et al., 2007; Cherniak and Zakharenkova, 2016; Katamazi-Joseph et al., 2017; Li et al., 2018; Aa et al., 2019).

Recently, Carrasco et al. (2020) studied the bifurcation of EPBs using a 2D Plasma Bubble Model (PBM2D) and found that this bifurcation was controlled by the polarization electric fields inside the EPB. According to their numerical simulations, the bifurcation is initiated once the head of the EPB has passed the F-layer's peak and when the maximum of the vertical field (positive) is very close to the minimum value of the zonal field in the middle part of the EPB. They also showed that the vertical electric field is bipolar inside the EPB and agrees with the electric field measurements reported by Aggson et al. (1996).

EPBs are one of the most significant issues of Space Weather on social lives, scattering and diffracting satellite-based navigation signals (e.g., Global Navigation Satellite System — GNSS), resulting in the wave signal's scintillations that can reduce the accuracy of GNSS signals, or even, in extreme cases, disable them. A large number of studies have been carried out during the last decades to understand better and improve the modeling and forecasting of EPBs, to mitigate the impact on society of these irregularities (Takahashi et al., 2016).

Nighttime medium-scale traveling ionospheric disturbances (MSTIDs) are wave-like perturbations in the ionospheric plasma. In the equatorial and low-latitude regions, nighttime MSTIDs are associated primarily with upward gravity waves related to tropospheric convective events (e.g., Fukushima et al., 2012). On the other hand, some events observed in the low latitude region are associated also with midlatitude nighttime MSTIDs, most of which are generated by electrodynamic forces due to Perkins instability (e.g., Amorim et al., 2011; Sivakandan et al., 2019). In general, midlatitude nighttime MSTIDs propagate northwestward (southwestward) in the Southern (Northern) hemisphere with a phase velocity from ~50 to 200 m/s, horizontal wavelengths of ~80 to 160 km, and periods ranging from ~5 to 45 minutes (Amorim et al., 2011; Figueiredo et al., 2018).

Some observed characteristics of Perkins instability, such as growth rate and propagation direction preference, are still not fully explained (e.g., Miller et al., 1997; Kelley and Miller, 1997). In the last two decades, Cosgrove et al. (2004), Otsuka et al. (2007), Yokoyama et al. (2009), Yokoyama and Hysell (2010) have proposed that the electrical coupling between the E- and F-regions can increase the growth rate of the Perkins instability and control the propagation direction of an MSTID.

The interaction between EPBs and TIDs has been the subject of several recent investigations. Otsuka et al. (2012) reported the disappearance of EPBs after interacting with an MSTID over Shigaraki (34.9°N, 136.1°E), Japan, on August 22, 2001. They observed OI 630.0 nm airglow emissions using an all-sky imager, and report that EPBs were propagating eastward while the MSTID propagated southwestward, with a northwest-southeast wavefront alignment. They suggest that the electric field associated with the MSTID shifts the ambient ionization plasma into EPBs, causing them to vanish.

Using simultaneous measurements of the OI 630.0 nm emission, made on August 8, 2002, by two all-sky imagers located at geomagnetically conjugate points — Darwin, Australia (12.4°S, 131°E) and Sata, Japan (31°N, 130.7°E) — Shiokawa et al. (2015) observed an equatorward EPB disappearance. However, the disappearance was observed only in the field of view of the Darwin imager. The authors suggested that an enhancement of the equatorward thermospheric wind, driven by an equatorward-propagating large-scale traveling ionospheric disturbance (LSTID) over Darwin, could explain the observations.

Narayanan et al. (2016a) studied some EPB cases over Panhala (16.8°N, 74.1°E), also using OI 630.0 nm emission. They observed a reduction in the latitudinal extension of the EPBs corresponding to downward drift over the magnetic equator. However, the authors have argued that these events seemed not to be related to TIDs. In another case, one EPB was shrinking while an adjacent EPB was growing. Since the longitudinal extension of a TID is significantly larger than a few kilometers, the TID should interact almost simultaneously with both EPBs. The authors found no conclusive explanation of the observed EPB shrinking. The interaction between EPBs and TIDs thus remains a complex and not well-understood subject with severe implications for nighttime ionosphere morphology and dynamics.

The present work aims to report observations of the interaction between EPBs and an MSTID by OI 630.0 nm airglow imaging — the first results obtained by the all-sky imager installed at Bom Jesus da Lapa observatory in Brazil. Details of the observed interaction between EPBs and an MSTID and a possible explanation will be presented in the following sections.

2. Instrumentation

A new airglow observatory was installed at Bom Jesus da Lapa (BJL) (13.3°S, 43.5°W; Quasi-Dipole (QD) latitude of 14.1°S) in December 2019, under a scientific collaboration between the National Institute for Space Research (INPE) and the Federal Institute of Education, Science and Technology Baiano (IF Baiano). The all-sky imager installed at the BJL observatory measures airglow emissions from the mesosphere and thermosphere regions. The observatory is strategically located under the Equatorial Ionization Anomaly (EIA) South crest, not far from the São João do Cariri (CA) (7.4°S, 36.6°W; QD: 12.7°S) observatory. Thus, these observatories allow excellent coverage of this area on the Brazilian coast to monitor the mesosphere and ionosphere dynamics.

The imager is composed of a fisheye lens, with a 180° field of view, a 3-inch diameter interference filter, a telecentric lens system, and an objective lens to project the image onto a Charged Coupled Device (CCD) camera, with an array of 1024 × 1024 pixels. Airglow measurements are made for the OI 557.7 nm, OI 630.0 nm, Hydroxyl (715–930 nm), and O_2 emissions. Image integration times are 15 seconds for OH and 90 seconds for OI 557.7 nm, OI 630.0 nm, and O_2.

This study also used a ground-based network of GNSS receivers to monitor EPBs and the EIA by mapping the Total Electron Content (TEC map). TEC is calculated using both phase delay and pseudo-range of the GNSS satellite dual-frequency radio signals. TEC values are mapped on an ionospheric shell at an altitude of 350 km, with a spatial resolution ranging from 50 to 500 km, depending on the GNSS receivers' density. This TEC map can cover almost the entire South America continent and monitor TEC variability continuously with a time resolution of 10 minutes (Takahashi et al., 2016; Barros et al., 2018).

A Digisonde Portable Sounder-4 (DPS4) ionosonde located at Fortaleza (FZ) (3.7°S, 38.6°W; QD: 8.7°S), Brazil, was also used to observe the structure and dynamics of F-layers. The DPS4 has a peak power of around 10 kW and average power of 500 W, transmitting electromagnetic pulses in a wide frequency range, from 0.5 to 30.0 MHz. This ionosonde uses an antenna transmitter, four antenna receivers, and a circuit to amplify the received echoes. After the reception, the signals are recorded as a diagram of the ionosphere's virtual height plotted against frequency, known as an ionogram. Virtual heights are calculated based on the time interval between pulse transmission and echo reception; the results are accurate to ±5 km (Reinisch et al., 1997).

Electron density and TEC profiles from GNSS Radio Occultation (RO) data, measured by Constellation Observing System for Meteorology, Ionosphere, and Climate (COSMIC-2), were also used. COSMIC-2 is an international collaboration between the National Space Organization (NSPO) from Taiwan and the National Oceanic and Atmospheric Administration (NOAA) from the United States. It uses a constellation of six remote sensing microsatellites to collect atmospheric data for weather prediction and for ionosphere, climate, and gravity research.

The RO is a conceptually simple remote sensing method that employs radio transmitter/receiver pairs with a signal path that transits a planetary limb. A GNSS receiver onboard a Low Earth Orbit (LEO) satellite allows precise measurements of the amplitude and phase of GNSS radio signals when the LEO satellite is occulted by Earth's ionosphere and atmosphere (Yue et al., 2014).

By assuming spherical symmetry, it is possible to determine the ionospheric electron density of the tangent point by using the Abel transform. After that, TEC values are calculated by integrating the electron density profile and mapping to the vertical direction. The derived range is from 80 km to the COSMIC satellite orbital height, around 800 km of altitude (Jakowski et al., 2005; Sun et al., 2017; Li et al., 2019). This paper used COSMIC-2 electron density and TEC values from the "ionPrf" files from the Level 1b Dataset, which are freely available on the web portal of the COSMIC Data Analysis and Archival Center (CDAAC, https://cdaac-www.cosmic.ucar.edu/) and databases of the Taiwan Analysis Center for COSMIC (TACC, https://tacc.cwb.gov.tw/v2/en/index.html/).

3. Results and Discussions

Figure 1 presents an OI 630.0 nm unwrapped image, obtained at the BJL observatory, by the all-sky imager at 01:19 UT on the night of September 16 to 17, 2020. The BJL airglow observatory is indicated as a dot and a label in the center of the image; the CA imager is depicted by a dot and a label in the upper right corner of the image. The ionosonde, located at FZ, is indicated as a green square. Radio occultation mean longitude and latitude measurements taken from COSMIC-2, are shown as a blue asterisk (7.5°S, 44.9°W; QD: 8.6°S) and orange triangle (11.8°S, 45.1°W; QD: 12.0°S) in Figure 1. The magnetic equator (at 250 km of altitude) is represented by a black line, while the magnetic field lines, and the quasi-dipole latitudes are depicted in red. It is possible to see the EIA south crest as a bright band in the northeast–southwest direction, and EPBs in the top side of the image, as narrow dark depletions in the north–south direction.

Figure 2 presents in Panels (I) and (II) the OI 630.0 nm relative intensity and detrended unwrapped images, respectively. Each detrended image was calculated by using a mean image obtained in the time interval of $(t - 30\ \text{min}) < t < (t + 30\ \text{min})$. The image sequence was obtained at the BJL observatory on the night of September 16 to 17, 2020. It is essential to mention that it was a geomagnetically quiet night.

Figure 2 (Panels I and II) records, between 01:19 UT and 02:16 UT, the occurrence of five EPBs, marked as B1, B2, B3, B4, and B5 in the images, moving eastward with a zonal drift velocity of 63 ± 7 m/s. On the other hand, a dark band MSTID, marked as M, propagates towards the group of EPBs, from southeast to northwest, with a phase velocity of 111 ± 6 m/s. Before the interaction between the EPB group and the MSTID, EPB B5 can be seen to bifurcate, from 01:19 UT to 02:16 UT; after which the bifurcation disappears.

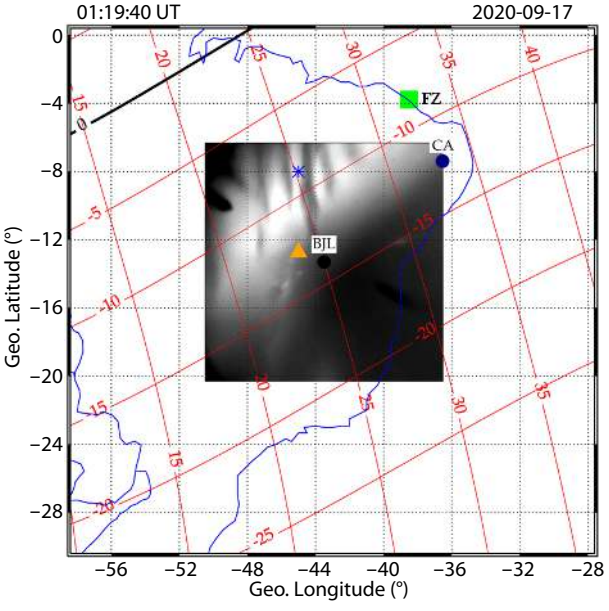

Figure 1. BJL OI 630.0 nm unwrapped image showing the EIA south crest and EPBs occurrence on the night of September 16 to 17, 2020, at 01:19 UT. BJL airglow observatory is indicated as a black dot in the center of the image. CA observatory is indicated as a blue dot. Ionosonde (FZ) and radio occultation mean longitude and latitude measurements taken from COSMIC-2 are shown by a green square, a blue asterisk, and an orange triangle. The black line represents the magnetic equator (at 250 km altitude); the red lines represent the magnetic field lines and the quasi-dipole latitude.

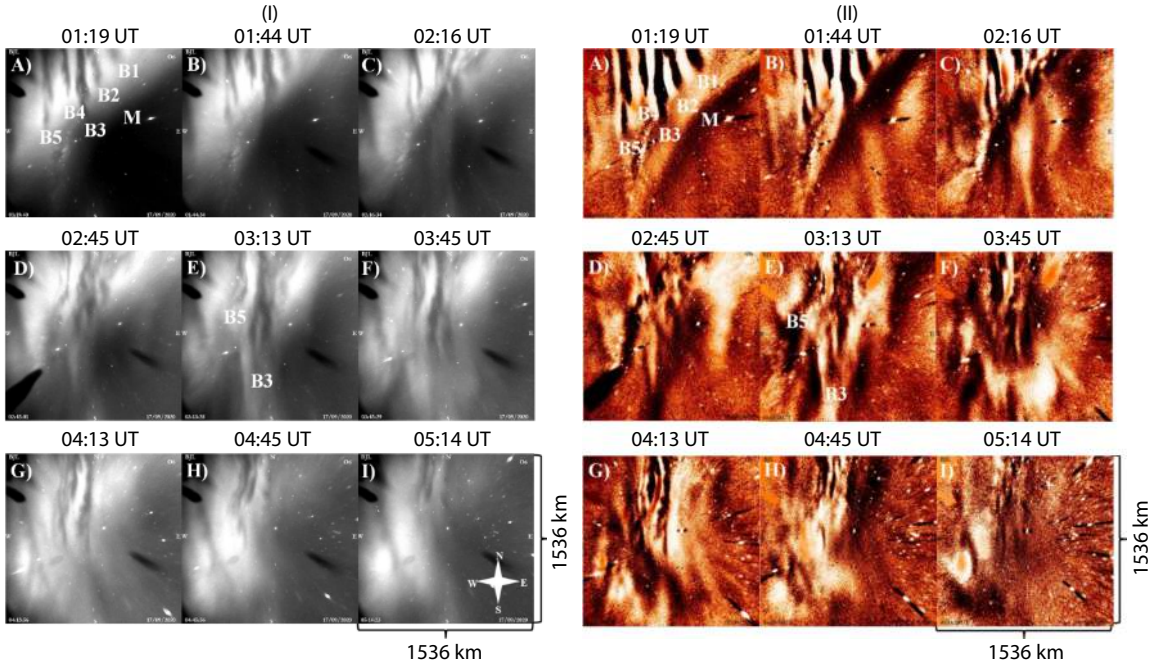

Figure 2. Panels (I) and (II) present the OI 630.0 nm relative intensity and detrended unwarped images obtained at Bom Jesus da Lapa Observatory (13.3°S, 43.5°W; QD: 14.1°S) showing the interaction between EPBs and MSTID on the night of September 16 to 17, 2020.

Around 02:16 UT, the EPBs interact with the MSTID; EPBs B3 and B4 are forced to merge (B3 + B4), followed by an abrupt southward development. From 03:13 UT, the combined EPB B3 + B4 bifurcates, and completely vanishes at 05:14 UT. The interaction of the MSTID with the EPBs at the beginning favors the development of EPB B3 + B4, and then later, inhibits the combined EPB. This is the first observation in which it has been possible to follow EPB evolution through phases of bifurcation and disappearance.

The pattern that emerges from our results may be summarized as follows: (1) The interaction between the polarization electric fields (zonal and vertical) produced inside the EPBs (Carrasco et al., 2020) and the electric fields associated with the MSTID (Otsuka et al., 2012) causes the abrupt growth of the EPBs (B5, B3+B4) and their bifurcation. (2) After electrostatic interaction, a mechanical interaction also occurs via charged particle density between the EPBs and the MSTID, which causes the bifurcation to disappear (see images at 02:16 UT and 04:13 UT), followed by the complete disappearance at 05:14 UT of all EPBs from the all-sky imager field of view.

The latitudinal growth of EPB B3 was also calculated; between 00:00 UT and 00:44 UT, EPB B3 decreased its latitudinal growth by 28 m/s. As the MSTID approached EPB B3 between 00:44 and 01:33 UT, B3 grew at 14 m/s as if it were drawn to the MSTID. Finally, when the MSTID interacted with EPB B3, it grew at a rate of 58 m/s. EPB B3 developed from the magnetic equator up to ~16°S (geographic latitude), corresponding to an Apex height of about 600 km. In our work, EPB drift velocity and propagation direction were obtained using a 2-D Fourier Transform (Wrasse et al., 2007). An animation showing the Figure 2 OI 630.0 nm image sequence is available through this paper's supporting information.

Based on the EPB B3 latitudinal growth velocities indicated above, it is possible that EPB B3 grew faster latitudinally as a result of its interaction with the MSTID. Therefore, we conclude that the MSTID's eastward polarizing electric field may play a significant role in EPB growth.

Using data from all-sky images, Narayana et al. (2016b) propose three different mechanisms to explain the merging of EPBs. One of the mechanisms they propose is defined as follows: the leading EPB slows down, the trailing EPB catches up, and they merge. In our case, the merging was slightly different; the electrified MSTID (eMSTID) changed the EPBs' velocities and forced EBP B2 and B4 to merge with B3. Consequently, the EPB B3's growth in latitude suggests an intensification of the eastward polarization electric field inside the EPBs.

EPBs are considered to move at approximately the same velocity as the ambient plasma drift (Sobral et al., 2009). During the daytime, the ionospheric electron density drifts under the influence of vertical electric fields generated by E- and F-region dynamos (Haerendel et al., 1992). During the nighttime, the E-region electron density undergoes by a rapid dissociative recombination (Heelis et al., 1974), and the F-region dynamo controls the dynamics of the ionosphere. EPBs observed at BJL in the OI 630.0 nm airglow images on September 16 to 17, 2020, were propagating eastward with a zonal drift velocity of around 63 ±7 m/s. Barros et al. (2018) describe characteristics of EPBs observed between November 2012 and January 2016 over South America using TEC maps based on ground-based GNSS receivers; they report that the EPBs exhibited an eastward movement with zonal drift velocities varying from 80 to 150 m/s at around 13°S geographic latitude. EPBs' zonal velocities found at BJL were slightly smaller than those observed by Barros et al. (2018). However, Sobral et al. (2009) pointed out that EPB zonal velocity increases with increased solar

flux. Moreover, the EPB zonal drift velocity depends on local time; velocity is observed to lessen toward local midnight. Besides the time difference between the measurements, a weaker EPB zonal velocity observed at the BJL observatory could be attributed to a weaker solar flux, which leads to weaker neutral wind and F region dynamo.

Besides the EPBs' occurrence, the EIA south crest is also seen as a bright band in the north–southwest direction of the all-sky images showed in Figure 2. The EIA south crest seems to disperse southwestward after 03:13 UT, followed by decreased OI 630.0 nm relative intensity — seen in Panel (I) of Figure 2f.

Figure 3 presents TEC maps at 01:20 UT and 03:40 UT on the night of September 16 to 17, 2020. The white circle indicates the BJL all-sky imager field of view. Occurrence of EPBs can be seen in Figure 3a, on the northwest side of the BJL all-sky imager field of view (marked by the dashed white lines). The TEC maps also clearly show the dynamics of the EIA South crest over BJL through the night (indicated by the white arrows). After approximately 03:40 UT (Figure 3b), the decrease of OI 630.0 nm relative intensity seen in Figure 2f can be explained by the low ionization in the EIA crest region. Despite that, the BJL all-sky imager could follow the EIA south crest, verifying that it remained above the BJL region throughout the entire night.

The EPBs were drifting eastward until they met the eMSTID at 02:16 UT, as shown in Figure 2c and in the supplementary material. After that, the EPBs merged, followed by an abrupt southward development. Otsuka et al. (2012) and Shiokawa et al. (2015) observed disappearances of an EPB after the interaction with the eMSTID and suggest that plasma velocity shear associated with the eMSTID filled the EPB inside the region with plasma due to $\boldsymbol{E}\times\boldsymbol{B}$ drift. However, the interaction between EPB and eMSTID in the present case suggests that the dark band eastward polarization electric field induced an enhancement of the EPB polarization electric field, causing further uplifting. Due to the magnetic field line's equipotential nature, the polarization electric field is mapped to different latitudes and altitudes. The EPBs developed almost ~500 km latitudinally, which correspond to ~200 km in Apex height.

We used FZ ionosonde data and CA all-sky images to analyze how the eMSTID's eastward polarization electric field affected the EPBs' behavior at BJL. The ionosonde observations are inside the all-sky imager field, so it is possible to calculate the eMSTID's polarization electric field *in situ*. Figure 4 shows, in Panels (I) and (II), the CA OI 630.0 nm relative intensity and detrended unwarped images, on September 16 to 17, 2020. The sequence of images shows two EPBs (B1 and B2) and the eMSTID (M), each at 30-minutes time intervals; the EPB and eMSTID interaction occurs at

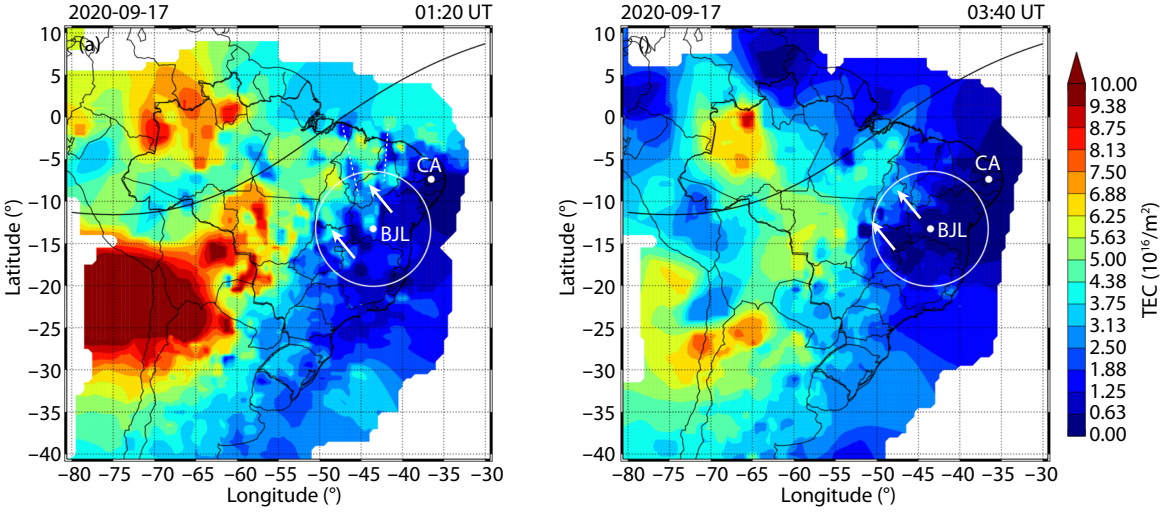

Figure 3. TEC maps at 01:20 UT and 03:40 UT on the night of September 16 to 17, 2020. TEC map show the occurrence of EPBs (white dashed lines) over the northwest side of the BJL all-sky imager field of view. White dots depict the locations of airglow observatories CA and BJL, while the arrows indicate the location of EIA south crest.

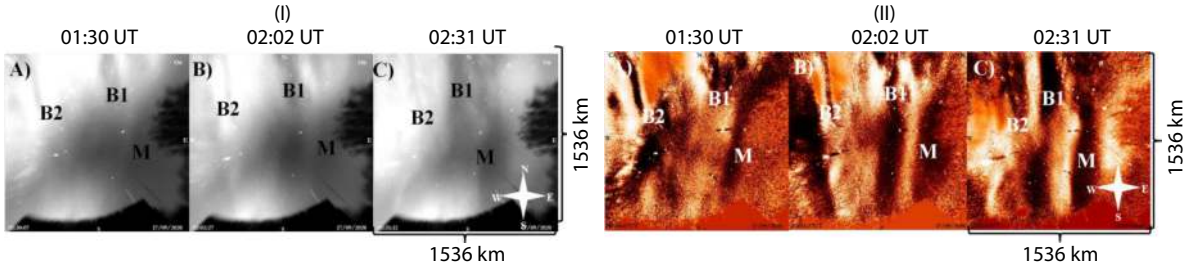

Figure 4. Panels (I) and (II) show the OI 630.0 nm relative intensity and detrended unwarped images taken at São João do Cariri (CA) observatory (7.4°S, 36.6°W; QD: 12.7°S) and also presents the interaction between EPBs and MSTID on the night of September 16 to 17, 2020.

02:02 UT. It is important to mention that the eMSTID observed at CA is the same one observed at BJL.

Figure 5 presents the FZ ionograms obtained at 01:50 UT and 03:30 UT, showing a difference of ~30 km in the F-layer virtual height (Reinisch and Huang, 1983; Huang and Reinisch, 1996; Huang, and Reinisch, 2001). This difference might be due to the influence of the eMSTID, which induces an enhancement in the F-region eastward electric field, forcing the F-layer to drift upward.

Figure 6 shows the ionospheric parameters measured by the FZ ionosonde on the night of September 14 to 15 (Panel I) and September 16 to 17 (Panel II), 2020. Panels (a) represent true height (*h*F) variations at fixed frequencies of 5, 6, and 7 MHz, while Panels (b) show the band-pass filtered oscillations (d(*h*F)/d*t*) of the fixed frequencies; Panels (c) show the eastward polarization elec-

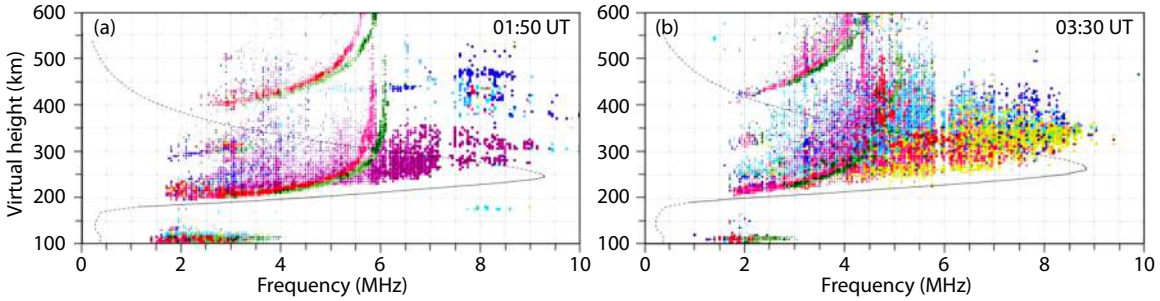

Figure 5. Ionograms obtained at Fortaleza (FZ) (3.7°S, 38.6°W; QD: 8.7°S) on the night of September 16 to 17, 2020, showing a height difference between the ionograms at 01:50 UT and 03:30 UT.

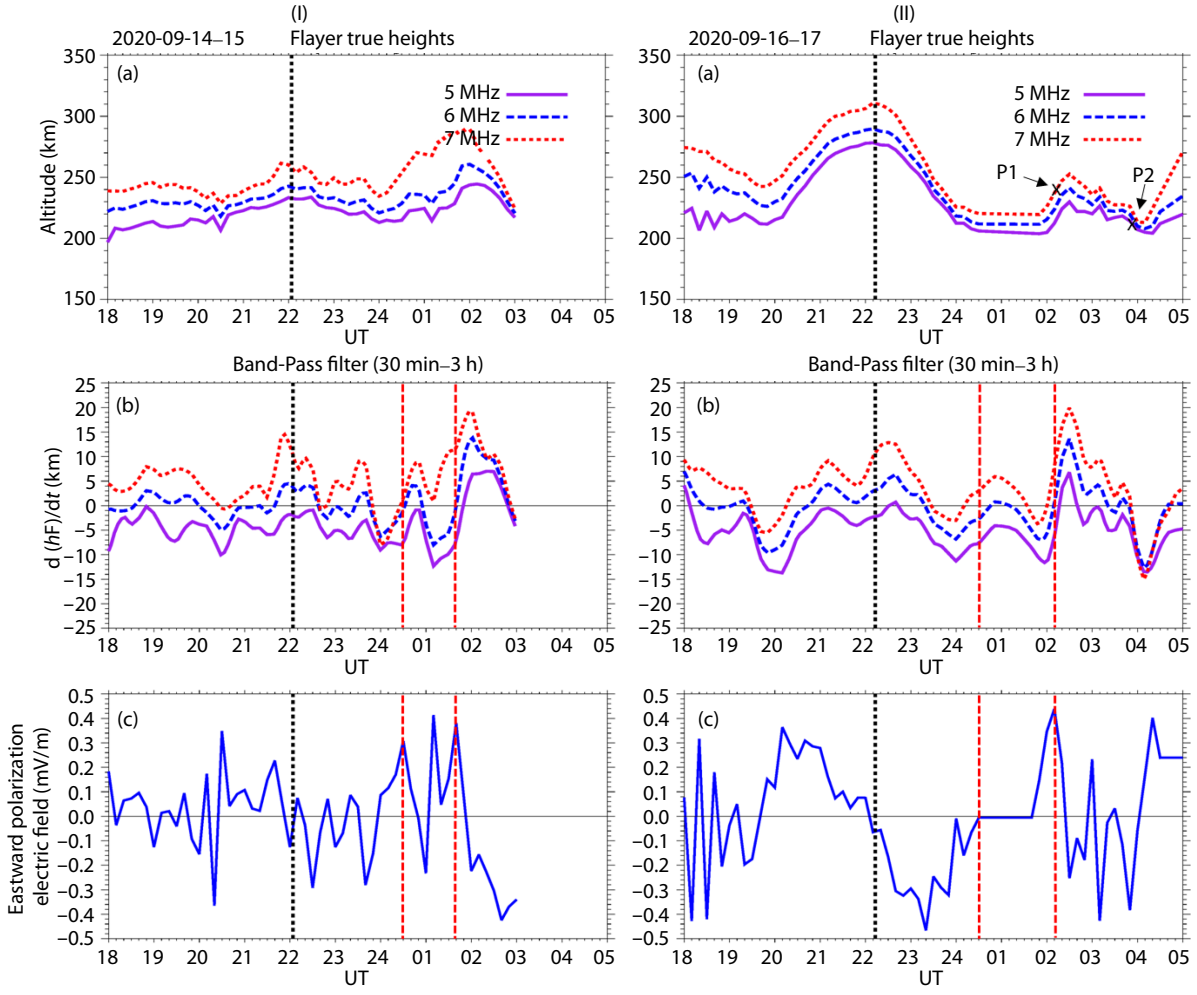

Figure 6. (a) True height variations at fixed frequencies of 5, 6, and 7 MHz; (b) the band-pass filtered oscillations (d(*h*F)/d*t*) of the fixed frequencies; (c) Eastward polarization electric field over FZ on the night of September 14 to 15 (Panel I) and September 16 to 17 (Panel II), 2020. The vertical black dotted line indicates the solar terminator at 350 km altitude. The vertical red dashed lines indicate the EPBs' occurrence. P1 and P2 depict the time of the RO measurements.

tric field. The vertical black dotted line indicates the solar terminator at 350 km altitude, while the vertical red dashed lines indicate the EPBs' occurrences. The night of September 14 to 15 (Panel I) was chosen for comparison with the results observed on September 16 to 17 (Panel II): note that on September 14 to 15 EPBs were observed, but in the absence of any MSTID. The intensity of the eastward polarization electric field (E_x) was estimated using the relation $\mathrm{d}(h\mathrm{F})/\mathrm{d}t \approx E_x/B$ (Abdu et al., 1981; Batista et al., 1986). $\mathrm{d}(h\mathrm{F})/\mathrm{d}t$ was calculated from the true height at the fixed frequencies of 5, 6, and 7 MHz; B was obtained from International Geomagnetic Reference Field (IGRF) 2020 (Thebault et al., 2015), at 250 km of altitude.

As proposed by several authors, wave-type structures seen in the ionospheric parameters could be associated with the occurrence of EPBs (e. g. Abdu et al. 2009, Tsunoda et al., 2018, Takahashi et al., 2018). On both days (Figure 6, Panels I and II) the wave structures observed are in good agreement with the occurrences of EPBs detected in CA OI 630.0 nm airglow images. The vertical red lines indicate the eastward polarization electric field behavior before the EPBs' occurrence. As pointed out by Abdu et al. (2009) and Resende et al. (2019), there is a time delay of a few minutes between the intensification of the polarization electric field associated with the F region vertical drifts and the occurrence of EPBs. The same time delay can be seen between the intensification of the polarization electric field and the wave structures peak associated with EPB occurrence.

On the night of September 16 to 17, all the frequencies oscillated in phase, with no time delay. Analyzing the polarization electric field associated with two consecutive EPBs (at 00:30 UT and 02:10 UT) and the eMSTID passage, a variation of ~0.4 mV/m can be seen in Panel II of Figure 6a. The increase of the polarization electric field is followed by an abrupt F-layer upward movement. However, on the previous night (September 14 to 15) the frequencies did not conform to the well-noticed in-phase oscillation. Moreover, that night the F-layer exhibited a smooth upward movement; analysis of the polarization electric field associated with the two consecutive September 14–15 EPBs (at 00:30 UT and 01:40 UT), reveals a variation of ~0.08 mV/m.

The polarization electric field variation associated with the two consecutive EPBs, at approximately the same time, on the night of September 16 to 17, was five times larger than polarization electric field variation on the previous night on which no eMSTID was observed. It thus seems likely that the abrupt movement seen on the night of September 16 to 17, 2020, can be related to the passage of the eMSTID.

The observational results presented in this paper entirely agree with the simulated results reported by Krall et al. (2011). Using The Naval Research Laboratory three-dimensional simulation code SAMI3/ESF, the authors investigated the response of the post-sunset F-layer to an eMSTID. They found that when the eMSTID encounters the field lines at the F-layer bottom side, the eastward polarization electric field associated with the eMSTID could trigger the EPB's growth.

Figure 7 presents electron density and TEC profiles obtained by COSMIC-2 satellite data on the night of September 16 to 17, 2020. Both electron density and TEC profiles measured by COSMIC-2 satellites show similar behavior observed by the ionosonde at FZ. The electron density profiles observed at 02:11 UT (solid red line) and 03:52 UT (dashed red line) present a peak height around ~270 and 235 km, respectively. On the other hand, TEC profiles observed at 02:11 UT (solid blue line) and 03:52 UT (dashed blue line) show a peak height at ~245 and ~215 km, respectively. The figure suggests a downward movement of the F-layer, similar to the F-layer downward movements seen in Panel II of Figure 6a, at 02:30 UT (P1) and 03:50 UT (P2). Moreover, electron density profiles and TEC values at the peak present a significant decrease from one measure to another. This decrease may be due to low electron density associated with EPBs, eMSTID, or EIA southwestward movement, seen in the TEC maps of Figure 3, or just merely a nighttime F layer decrease.

After the EPB's abrupt southward grow (shown in Figure 2), it presents a well-developed bifurcation due to its interaction with the eMSTID. The bifurcation phenomenon has been studied by several authors using both observational and numerical methods (Aggson et al., 1996; Huang and Kelly, 1996; Hysell, 1999; McDonald et al., 1981; Yokoyama et al., 2014; Zalesak et al., 1982). Recently, Carrasco et al. (2020) used a numerical simulation to analyze several theories in the EPB bifurcation literature; they report that EPB bifurcation at the magnetic equator is initiated once the head of the EPB has passed the F-layer's peak and when the maximum of the vertical field (positive and inside the EPB) is very close to the minimum value of the zonal field in the middle part of the EPB.

Observations from satellites (Aggson et al., 1996) and numerical simulation (Carrasco et al., 2020) have both shown that inside an EPB at the magnetic equator, the electric field's zonal and vertical

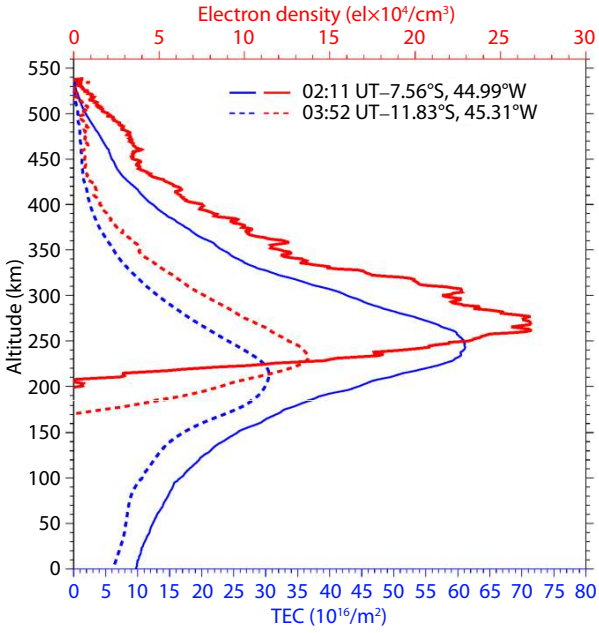

Figure 7. Electron density (red) and TEC (blue) profiles measured by COSMIC-2 satellites on the night of September 16 to 17, 2020, near the BJL airglow observatory. Solid and dashed lines represent the occultation at 02:11 UT and 03:52 UT.

components can present an unipolar and bipolar variation, respectively. Inside such an EPB, while the zonal electric field drifts the electron density upward, the vertical electric field separates the electron density towards the EPB walls, causing the bifurcation. However, the bifurcation observed in our airglow images corresponds to latitudes outside the magnetic equator. Therefore, a more detailed analysis is necessary to explain the bifurcation process reported here, seen over the BJL observatory. The growth of EPBs along the magnetic tube plays an important role in the dynamics of the EPBs, which must be taken into account in numerical simulation of theoretical models.

Finally, we compare the current results to the case study reported by Otsuka et al. (2012). In Otsuka's case, the disappearance of the EPB was attributed to the associated polarization electric field of the eMSTID. However, in the case reported here, from observations taken under low solar flux conditions, an EPB with low latitudinal extension experienced additional elongation and bifurcation when interacting with an eMSTID, an interaction that had two distinct characteristics: first, the polarization electric field is mapped to the equator, contributing to the EPB growth; second, the fading effect may be related to an increase in the EPB's height due to the eMSTID interaction, which is equivalent to a northward transequatorial wind. Therefore, the EPB in the present study is unique, with different characteristics from those in the case presented by Otsuka et al. (2012).

4. Conclusions

We describe the interaction between EPBs and the eMSTID on the night of September 16 to 17, 2020, the first study based on data obtained at the Bom Jesus da Lapa (BJL) airglow observatory in Brazil. The EPBs were drifting eastward in an apparent "fossil" stage until they encountered the dark band eMSTID. After that, four EPBs merged, followed by an abrupt southward development. Also observed in the EPBs was well-developed bifurcation. Our analysis suggests that an eastward polarization electric field induced by the dark band eMSTID mapped along the magnetic field lines, forcing the EPBs to drift upward, originating elongation along the magnetic field lines and giving rise to bifurcation.

Acknowledgment

The airglow images data used in this study were provided by Embrace/INPE (http://www2.inpe.br/climaespacial/portal/linearim-agevideo/). The authors would like to thank the IF Baiano for supporting and maintaining the Bom Jesus da Lapa airglow observatory. The present work was supported by Coordenação de Aperfeiçoamento de Pessoal de Nível Superior (CAPES) and by Conselho Nacional de Desenvolvimento Científico e Tecnológico (CNPq), under the processes 470589/2012-4, 305461/2015-0, 303511/2017-6, 307653/2017-0, and 169815/2017-0. C.A.O.B. Figueiredo thanks to the Fundação de Amparo à Pesquisa do Estado de São Paulo (FAPESP) under the process 2018/09066-8. L. C. A. Resende would like to thank the China-Brazil Joint Laboratory for Space Weather (CBJLSW), National Space Science Center (NSSC), Chinese Academy of Sciences (CAS) for supporting her postdoctoral research.

References

Aa, E., Zou, S., Ridley, A., Zhang, S. R., Coster, A. J., Erickson, P. J., Liu S. Q., and Ren, J. E. (2019). Merging of storm time midlatitude traveling ionospheric disturbances and equatorial plasma bubbles. *Space Weather*, *17*, 285–298. https://doi.org/10.1029/2018SW002101

Abdu, M. A. (2001). Outstanding problems in the equatorial ionosphere–thermosphere electrodynamics relevant to spread F. *Journal of Atmospheric and Solar-Terrestrial Physics*, *63*(9), 869–884. https://doi.org/10.1016/S1364-6826(00)00201-7

Abdu, M. A., Batista, I. S., and Bittencout, J. A. (1981). Some characteristics of equatorial spread F at the magnetic equatorial station Fortaleza. *Journal of Geophysical Research*: *Space Physics*, *86*(A8), 6836–6842. https://doi.org/10.1029/JA086iA08p06836

Abdu, M. A., Medeiros, R. T., Sobral, J. H. A., and Bittencourt, J. A. (1983). Spread F Plasma bubble vertical rise velocities determined from space ionosonde observations. *Journal of Geophysical Research*: *Space Physics*, *88*(A11), 9197–9204. https://doi.org/10.1029/JA088iA11p09197

Abdu, M. A., Batista, I. S., Reinisch, B. W., Souza, J. R. de, Sobral, J. H. A., Pedersen, T. R., Medeiros, A. F., Schuch, N. J., Paula, E. R. de, and Groves, K. M. (2009). Conjugate Point Equatorial Experiment (COPEX) campaign in Brazil: Electrodynamics highlights on spread F development conditions and day-to-day variability. *Journal of Geophysical Research*, *114*(A4), A04308. https://doi.org/10.1029/2008JA013749

Aggson, T. L., Laakso, H., Maynard, N. C., and Pfaff, R. F. (1996). In situ observations of bifurcation of equatorial ionospheric plasma depletions. *Journal of Geophysical Research*, *101*(A3), 5125–5132. https://doi.org/10.1029/95JA03837

Amorim, D. C. M., Pimenta, A. A., Bittencourt, J. A., and Fagundes, P. R. (2011). Long term study of medium-scale traveling ionospheric disturbances using oi 630 nm All-Sky imaging and ionosonde over Brazilian low latitudes. *Journal of Geophysical Research*, *116*, A06312. https://doi.org/10.1029/2010JA016090

Barros, D., Takahashi, H., Wrasse, C. M., and Figueiredo, C. A. O. B. (2018). Characteristics of equatorial plasma bubbles observed by TEC map based on ground-based GNSS receivers over South America. *Annales Geophysicae*, *36*(1), 91–100. https://doi.org/10.5194/angeo-36-91-2018

Batista, I. S., Abdu, M. A., and Bittencourt, J. A. (1986). Equatorial F region vertical plasma drifts: Seasonal and longitudinal asymmetries in the American sector. *Journal of Geophysical Research*, *91*, 12,055–12,064. https://doi.org/10.1029/JA091iA11p12055

Carrasco, A. J., Pimenta, A. A., Wrasse, C. M., Batista, I. S., and Takahashi, H. (2020). Why do equatorial plasma bubbles bifurcate?. *Journal of Geophysical Research*: *Space Physics*, *125*, e2020JA028609. https://doi.org/10.1029/2020JA028609

Carrasco, A. J., Batista, I. S., Sobral, J. H. A., and Abdu, M. A. (2017). Spread F modeling over Brazil. *Journal of Atmospheric and Solar-Terrestrial Physics*, *161*, 98–104. https://doi.org/10.1016/j.jastp.2017.06.015

Cosgrove, R. B., and Tsunoda, R. T. (2004). Instability of the E-F coupled nighttime midlatitude ionosphere. *Journal of Geophysical Research*, *109*, A04305. https://doi.org/10.1029/2003JA010243

Cherniak, I., and Zakharenkova, I. (2016). First observations of super plasma bubbles in Europe. *Geophysical Research Letters*, *43*, 11,137–11,145. https://doi.org/10.1002/2016GL071421

Figueiredo, C. A. O. B., Takahashi, H., Wrasse, C. M., Otsuka, Y., Shiokawa, K., and Barros, D. (2018). Investigation of nighttime MSTIDS observed by optical thermosphere imagers at low latitudes: Morphology, propagation direction, and wind filtering. *Journal of Geophysical Research*: *Space Physics*, *123*, 7843–7857. https://doi.org/10.1029/2018JA025438

Fukushima, D., Shiokawa, K., Otsuka, Y., and Ogawa, T. (2012). Observation of equatorial nighttime medium-scale traveling ionospheric disturbances in 630-nm airglow images over 7 years. *Journal of Geophysical Research*, *117*(A10324). https://doi.org/10.1029/2012JA017758

Haerendel, G. (1973). Theory of equatorial spread-F, Report Max-Planck Institute.

Haerendel, G., Eccles, J. V., and Çakir, S. (1992). Theory for modelling the equatorial evening ionosphere and the origin of the shear in the horizontal plasma flow. *Journal of Geophysical Research*: *Space Physics*, *97*, 1209–1223. https://doi.org/10.1029/91JA02226

Heelis, R. A., Kendall, P. C., Moffett, R. J., Windle, D. W., and Rishbeth, H. (1974). Electrical coupling of the E- and F- regions and its effect on F-region drifts and winds. *Planetary and Space Science*, *22*(5), 743–756. https://doi.org/10.1016/0032-0633(74)90144-5

Huang, C. S., and Kelley, M. C. (1996). Nonlinear evolution of equatorial spread F: Gravity wave seeding of Rayleigh-Taylor instability. *Journal of Geophysical Research*: *Space Physics*, *101*, 293–302. https://doi.org/10.1029/95JA02210

Huang, C.S., Foster, J. C. and Sahai, Y. (2007). Significant depletions of the ionospheric plasma density at middle latitudes: A possible signature of equatorial spread F bubbles near the plasmapause. *Journal of Geophysical Research*: *Space Physics*., *112*, A05315. https://doi.org/10.1029/2007JA012307

Huang, X., and Reinisch, B. W. (1996). Vertical electron density profiles from the Digisonde network. *Advances in Space Research*, *18*(6), 121–129. https://doi.org/10.1016/0273-1177(95)00912-4

Huang, X., and Reinisch, B. W. (2001). Vertical electron content from ionograms in real time. *Radio Science*, *36*(2), 335–342. https://doi.org/10.1029/1999RS002409

Hysell, D. L. (1999). Imaging coherent backscatter radar studies of equatorial spread F. *Journal of Atmospheric and Solar-Terrestrial Physics*, *61*, 701–716. https://doi.org/10.1016/S1364-6826(99)00020-6

Jakowski, N., Tsybulyal K., Stankov S.M., and Wehrenpfennig, A. (2005). About the Potential of GPS Radio Occultation Measurements for Exploring the Ionosphere. In: Reigber C., Lühr H., Schwintzer P., Wickert J. (eds). Earth Observation with CHAMP. Springer, Berlin, Heidelberg. https://doi.org/10.1007/3-540-26800-6_69

Katamzi-Joseph, Z. T., Habarulema, J. B., and Hernández-Pajares, M. (2017). Midlatitude postsunset plasmabubbles observed over Europeduring intense storms in April2000 and 2001. *Space Weather*, *15*, 1177–1190. https://doi.org/10.1002/2017SW001674

Kelley, M. C. (2009). *The Earth's Ionosphere*. Elsevier.

Kelley, M. C., and Miller, C. A. (1997). Electrodynamics of midlatitude spread F: 3. Electrohydrodynamic waves? A new look at the role of electric fields in thermospheric wave dynamics. *Journal of Geophysical Research*: *Space Physics*, *102*(A6), 11,539–11, 547. https://doi.org/10.1029/96JA03841

Krall, J., Huba, J. D., Ossakow, S. L., Joyce, G., Makela, J. J., Miller, E. S., and Kelley, M. C. (2011). Modeling of equatorial plasma bubbles triggered by non-equatorial traveling ionospheric disturbances. *Geophysical Research Letters*, *38*(8), L08103. https://doi.org/10.1029/2011GL046890

Li, G. Z., Ning, B. Q., Wang, C., Abdu, M. A., Otsuka, Y., Yamamoto, M., Wu, J., Chen, J. S. (2018). Storm-enhanced development of postsunset equatorial plasma bubbles around the meridian 120°E/60°W on 7–8 September 2017. *Journal of Geophysical Research*: *Space Physics*, *123*, 7985–7998. https://doi.org/10.1029/2018JA025871

Li, W., Huang, L., Zhang, S., and Chai, Y. (2019). Assessing Global Ionosphere TEC Maps with Satellite Altimetry and Ionospheric Radio Occultation Observations. *Sensors*, *19*(24), 5489. https://doi.org/10.3390/s19245489

McDonald, B. E., Ossakow, S. L., Zalesak, S. T., and Zabusky, N. J. (1981). Scale sizes and lifetimes of F region plasma cloud striations as determined by the condition of marginal stability. *Journal of Geophysical Research*: *Space Physics*, *86*(A7), 5775–5784. https://doi.org/10.1029/JA086iA07p05775

Miller, C. A., Swartz, W. E., Kelley, M. C., Mendillo, M., Nottingham, D., Scali, J., and Reinisch, B. (1997). Electrodynamics of midlatitude spread F: 1. Observations of unstable, gravity wave-induced ionospheric electric fields at tropical latitudes. *Journal of Geophysical Research*: *Space Physics*, *102*(A6), 11,521–11,532. https://doi.org/10.1029/96JA03839

Narayanan, V. L., Gurubaran, S., Shiokawa, K., and Emperumal, K. (2016a). Shrinking equatorial plasma bubbles. *Journal of Geophysical Research*: *Space Physics*, *121*(7), 6924–6935. https://doi.org/10.1002/2016JA022633

Narayanan, V. L., Gurubaran, S., and Shiokawa, K. (2016b). Direct observational evidence for the merging of equatorial plasma bubbles. *Journal of Geophysical Research*: *Space Physics*, *121*, 7923–7931. https://doi.org/10.1002/2016JA022861

Otsuka, Y., Onoma, F., Shiokawa, K., Ogawa, T., Yamamoto, M., and Fukao, S. (2007). Simultaneous observations of nighttime medium-scale traveling ionospheric disturbances and e region field-aligned irregularities at midlatitude. *Journal of Geophysical Research*, *112*, A06317. https://doi.org/10.1029/2005JA011548

Otsuka, Y., Shiokawa, K., Ogawa, T., and Wilkinson, P. (2002). Geomagnetic conjugate observations of equatorial airglow depletions. *Geophysical Research Letters*, *29*(15), 43.1–4. https://doi.org/10.1029/2002GL015347

Otsuka, Y., Shiokawa, K., and Ogawa, T. (2012). Disappearance of equatorial plasma bubble after interaction with mid-latitude medium-scale traveling ionospheric disturbance. *Geophysical Research Letters*, *39*(14), L14105. https://doi.org/10.1029/2012GL052286

Pimenta, A. A., Bittencourt, J., Fagundes, P., Sahai, Y., Buriti, R., Takahashi, H., and Taylor, M. J. (2003). Ionospheric plasma bubble zonal drifts over the tropical region: a study using OI 630nm emission all-sky images. *Journal of Atmospheric and Solar-Terrestrial Physics*, *65*(10), 1117–1126. https://doi.org/10.1016/S1364-6826(03)00149-4

Reinisch, B. W., Haines, D. M., Bibl, K., Galkin, I., Huang, X., Kitrosser, D. F., Sales, G. S., and Scali, J. L. (1997). Ionospheric sounding support of OTH radar. *Radio Science*, *32*(4), 1681–1694. https://doi.org/10.1029/97RS00841

Reinisch, B. W., and Huang, X. (1983). Automatic calculation of electron density profiles from digital ionograms: 3. Processing of bottomside ionograms. *Radio Science*, *18*(4), 477–492. https://doi.org/10.1029/RS018i003p00477

Resende, L. C. A., Denardini, C. M., Picanço, G. A. S., Moro, J., Barros, D., Figueiredo, C. A. O. B., and Silva, R. P. (2019). On developing a new ionospheric plasma index for Brazilian equatorial F region irregularities. *Ann. Geophys.*, *37*, 807–818. https://doi.org/10.5194/angeo-37-807-2019

Sivakandan, M., Chakrabarty, D., Ramkumar, T. K., Guharay, A., Taori, A., and Parihar, N. (2019). Evidence for deep ingression of the midlatitude MSTID into as low as ~3.5° magnetic latitude. *Journal of Geophysical Research*: *Space Physics*, *124*, 749–764. https://doi.org/10.1029/2018JA026103

Sobral, J. H. A., Abdu, M. A., Batista, I. S., Zamlutti, C. J., and Borba, G. L. (1981). Wave disturbances in the low latitude ionosphere and equatorial ionospheric plasma depletions. *Journal of Geophysical Research*, *86*(A3), 1374–1378. https://doi.org/10.1029/JA086iA03p01374

Shiokawa, K., Otsuka, Y., Lynn, K. J. W., Wilkinson, P., and Tsugawa, T. (2015). Airglow-imaging observation of plasma bubble disappearance at geomagnetically conjugate points. *Earth Planets Space*, *67*(43), 1–12. https://doi.org/10.1186/s40623-015-0202-6

Sobral, J. H. A., Abdu, M. A., Pedersen, T. R. , Vivian M. Castilho, V. M., Arruda, D. C. S., Muella, M. T. A. H., Batista, I. S., Mascarenhas, M., Paula, E. R. de, … Bertoni, F. C. P. (2009). Ionospheric zonal velocities at conjugate points over Brazil during the Copex campaign: Experimental observations and theoretical validations. *Journal of Geophysical Research*: *Space Physics*, *114*(A4), A04309. https://doi.org/10.1029/2008JA013896

Sun, Y.Y., Liu, J.Y., Tsai, H. F., and Krankowski, A. (2017). Global ionosphere map constructed by using total electron content from ground-based GNSS receiver and FORMOSAT-3/COSMIC GPS occultation experiment. *GPS Solut*, *21*, 1583–1591. https://doi.org/10.1007/s10291-017-0635-4

Takahashi, H., Wrasse, C. M., Denardini, C. M., Pádua, M. B., Paula, E. R. de, Costa, S. M. A., Otsuka, Y., Shiokawa, K., Galera Monico, J. F., Ivo, A., Sant'Anna, N. (2016). Ionospheric TEC weather map over South America. *Space Weather*, *14*(11), 937–949. https://doi.org/10.1002/2016SW001474

Takahashi, H., Wrasse, C. M., Figueiredo, C. A. O. B., Barros, D., Abdu, M. A., Otsuka , Y., and Shiokawa, K. (2018). Equatorial plasma bubble seeding by MSTIDs in the ionosphere. *Prog Earth Planet Sci.*, *5*, 32. https://doi.org/10.1186/s40645-018-0189-2

Thébault, E., Finlay, C. C., Beggan, C. D., Alken, P., Aubert, J., Barrois, O., Bertrand, F., Bondar, T., Boness, A., … Zvereva T. (2015). International geomagnetic reference field: The 12th generation. *Earth, Planets and Space*, *67*(1), 79–91. https://doi.org/10.1186/s40623-015-0228-9

Tsunoda, R. T., Saito, S., and Nguyen, T. T. (2018). Post-sunset rise of equatorial F

layer — or upwelling growth?. *Prog Earth Planet Sci.*, *5*, 22. https://doi.org/10.1186/s40645-018-0179-4

Wrasse, C. M, Takahashi, H., Medeiros, A. F., Lima, L. M., Taylor, M. J, Gobbi, D., and Fechine, J. (2007). Determinação dos parâmetros de ondas de gravidade através da análise espectral de imagens de aeroluminescência. *Revista Brasileira de Geofísica*, *25*(3), 257–265. https://doi.org/10.1590/S0102-261X2007000300003

Yokoyama, T., and Hysell, D. L. (2010). A new midlatitude ionosphere electrodynamics coupling model (MIECO): Latitudinal dependence and propagation of medium-scale traveling ionospheric disturbances. *Geophysical Research Letters*, *37*(8), L08105. https://doi.org/10.1029/2010GL042598

Yokoyama, T., Hysell, D. L., Otsuka, Y., and Yamamoto, M. (2009). Three-dimensional simulation of the coupled Perkins and Es-layer instabilities in the nighttime midlatitude ionosphere. *Journal of Geophysical Research*, *114*(A3), A03308. https://doi.org/10.1029/2008JA013789

Yokoyama, T., Shinagawa, H., and Jin, H. (2014). Nonlinear growth, bifurcation, and pinching of equatorial plasma bubble simulated by three-dimensional high-resolution bubble model. *Journal of Geophysical Research*: *Space Physics*, *119*(10), 10474–10482. https://doi.org/10.1002/2014JA020708

Yue, X., Schreiner, W. S., Pedatella, N., Anthes, R. A., Mannucci, A. J., Straus, P. R., and Liu, J.-Y. (2014). Space weather observations by GNSS radio occultation: From FORMOSAT-3/COSMIC to FORMOSAT-7/COSMIC-2. *Space Weather*, *12*(11), 616–621. https://doi.org/10.1002/2014SW001133

Zalesak, S. T., Ossakow, S. L., and Chaturvedi, P. K. (1982). Nonlinear equatorial spread F: The effect of neutral winds and background Pedersen conductivity. *Journal of Atmospheric and Terrestrial Physics*, *77*(A1), 151–166. https://doi.org/10.1029/JA087iA01p00151